A Novel Method to Predict the Real Operation of Ferrite Inductors With Moderate Saturation in Switching Power Supply Applications

Giulia Di Capua, *Member, IEEE*, and Nicola Femia, *Senior Member, IEEE*

***Abstract*—This paper presents a method to predict the real operation current wave-shape of Ferrite Core (FC) inductors in switching power supply applications involving a moderate inductor saturation. The method is based on a behavioral analytical model of inductance versus current saturation curve, obtained starting from the data provided by inductors manufacturers. The algorithm developed to solve the nonlinear model of the inductor can be applied to predict the range of the operating conditions involving a sustainable partial saturation for FC inductors, and the resulting method is best suited for the selection of minimum size inductors for high-power-density power supply design solutions.**

***Index Terms*—Ferrite Cores, inductors, losses, saturation.**

NOMENCLATURE

$V_{\rm in}, V_{\rm out}$	Input voltage and output voltage.
v_{Lr}, i_{Lr}	Inductor voltage and current in [0, DT_s].
v_{Lf}, i_{Lf}	Inductor voltage and current in $[DT_s, T_s]$.
V_F	Diode voltage drop.
$R_{\rm ds}$	MOSFET drain-to-source on resistance.
$I_{\rm out}$	Output current.
$L_{\rm nom}$	Nominal inductance value of the inductor.
L_0	Inductance value for zero current.
$L_{\rm deepsat}$	Inductance value in deep saturation.
A_c	Magnetic core cross section area.
n	Winding turns number.
l_g, l_c	Air gap and magnetic path length.
μ_0, μ_r	Air and relative permeability.
$\Re_g$, $\Re_c$	Core and air gap reluctance.
$\Delta i_{L\rm pp}$	Inductor peak-to-peak current ripple.
$I_{L,\rm av}$	Inductor average current.
i_{L0}, i_{LD}, i_{LTs}	Inductor current in $t = 0$, $t = DT_s$ and $t = T_s$.
D	Converter main switch duty cycle.
T_s	Switching period.
f_s	Switching frequency.

I. INTRODUCTION

THE minimization of power inductors is one of the major problems in high-power-density switch-mode power supply (SMPS) design, especially using integrated inductors in SMPS system-on-chip (SoC) solutions [1]–[5]. Both in SoC and in traditional discrete SMPS solutions, losses and consequent temperature rise are the main intrinsic issues of power inductors operation. In [6], it was shown that in a power transformer for SMPS applications, the total losses are influenced by the form factor of the magnetic core rather than just by the core volume. The findings of [6] include the simpler case of a power inductor. Therefore, the fundamental problem to solve is how to find the most convenient magnetic component complying with the functional operation of the converter (control, protections) and providing the most appropriate tradeoff among losses, size, and cost. This investigation has necessarily to account for inductor saturation. Powdered iron cores (PICs) and Ferrite Cores (FCs) are primarily used in power inductors applications, specifically in SMPS inductors, chokes, transformers and filters [7]–[9]. For SMPS designs using discrete parts, a large variety of FC and PIC inductors are available from magnetic parts manufacturers, with different core materials and sizes, inductance values, windings resistance, and temperature rise. FCs usually are the first choice for high-efficiency designs, thanks to the resulting low losses [10]–[12]. However, FC inductors suffer from a pretty sharp inductance drop around a certain value of the current. For this reason, FC inductors are typically chosen so that their operating current has a maximum peak value lower than the current corresponding to the 30% of inductance drop with respect to the inductance nominal value.

In recent years, inductor saturation has been the subject of several scientific investigations [13]–[16]. Some authors have experimentally verified that smaller volume inductors working in partial saturation could help in achieving more compact SMPSs with an acceptable amount of power losses [15]. In view of that, several manufacturers have started to provide more data and more detailed inductance versus current curves for their magnetic parts [17], [18]. However, both in the scientific literature and in the manufacturers' application notes, no practical hints are available on how to predict of the real magnitude of the current ripple for FC inductors working in partial saturation and how to efficiently analyze the sustainability of such operating conditions. Moreover, a lot of innovative research has been produced on new possible technologies for the fabrication of on-chip integrated inductor structures [1], [19], [20], but just few literature references discuss the manner to deal with the nonlinear behavior of the power inductors [21]–[23]. Some authors have shown how to operate with voltage-controlled techniques [24], [25], in order to practically realize magnetoelectric inductors with variable inductance values, ideal for tunable inductor application. Other authors have discussed how to use soft-saturation magnetic materials, so as to jointly provide

Manuscript received June 7, 2014; revised October 12, 2014, December 16, 2014, and April 18, 2015; accepted May 26, 2015. Date of publication June 1, 2015; date of current version November 16, 2015. Recommended for publication by Associate Editor C. R. Sullivan.

The authors are with Dept. of Information Eng., Electrical Eng. and Applied Math. University of Salerno, 84084 Fisciano, Italy (e-mail: gdicapua@unisa.it; femia@unisa.it).

Color versions of one or more of the figures in this paper are available online at http://ieeexplore.ieee.org.

Digital Object Identifier 10.1109/TPEL.2015.2438952

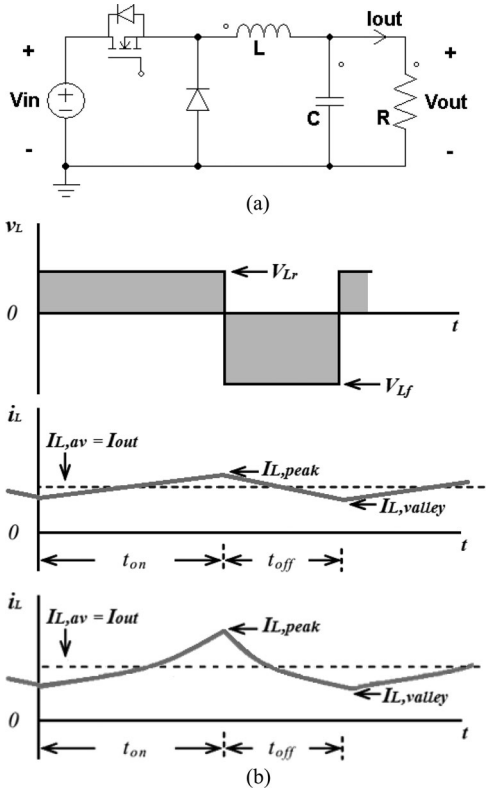

Fig. 1. (a) Buck converter and (b) relevant inductor current waveforms: from the top, voltage waveform, current waveform in weak saturation and in roll-off operating condition.

significant size reduction and acceptable efficiency in the magnetic design [26]. Also, new digital control techniques and enhanced intelligent control methods of the inductance value of power inductors have been recently investigated [27]–[29]. However, no suggestions or methods are available on how to quantify the benefit of a magnetic part working in a moderate and controlled saturation.

This paper discusses a novel generalized method to analyze the behavior of power inductors in SMPS applications. In particular, the proposed technique allows us to investigate power inductor operation including possible operation in saturation, with a reliable evaluation of the current ripple. Given the converter topology and its relevant specifications, the proposed method permits to compare different inductors and to select among them the best solution in terms of volume versus losses tradeoff. In Section II, the numerical technique for the reliable prediction of windings current wave-shape in FC inductors is proposed. In Section III, the temperature influence on FC inductors characteristics is described. In Section IV, experimental verifications are presented, showing an excellent agreement with the predictions of the proposed model.

II. Analysis of FC Inductors Operation

The analysis of FC inductors is herein referred to the buck converter of Fig. 1 operating in continuous conduction mode (CCM). Buck converter in CCM is of great interest for inductor saturation, especially because it is often operated at very high currents in point of load applications. Nevertheless, the proposed concepts, models and methods can be extended to other topologies and operating modes. The main quantities relevant to inductor current analysis for a buck converter in CCM are listed in Table I. Fig. 2 shows a typical inductance versus current curve for an FC inductor. Fig. 2 also highlights the current I_L^*, such that $L\left(I_L^*\right) = 0.5\left(L_{\rm nom} + L_{\rm deepsat}\right)$. For gapped core inductors, the deep saturation inductance $L_{\rm deepsat}$ is about from 10% to 20% of $L_{\rm nom}$ [17], [18]. Accordingly, three regions of operation can be identified:

- the weak saturation region, wherein the inductance slightly decreases respect to $L_{\rm nom}$, until about 70% of $L_{\rm nom}$;
- the deep saturation region, wherein the inductance is much lower than about 30% of $L_{\rm nom}$ and approaches $L_{\rm deepsat}$;
- the roll-off region, wherein the inductance swings from values close to $L_{\rm nom}$ to values close to $L_{\rm deepsat}$.

TABLE I
Modulation Schemes for Comparison

V_{Lr}	V_{Lf}	D
V_{in} -$R_{ds}I_{out}$ -V_{out}	- V_{out} -V_F	$(V_{out}+V_F)/(V_{in}$ -$R_{ds}I_{out}+V_F)$

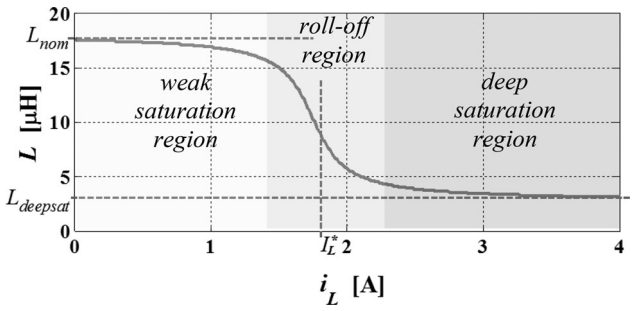

Fig. 2. Inductance versus current curve for an FC inductor.

The buck converter achieves output voltage regulation thanks to a controller, which adjusts the duty cycle until the difference of the output voltage respect to the desired nominal value is nulled, or reduced below a certain acceptable accuracy. Whatever control technique is implemented, the controller ensures the desired output voltage regulation in steady-state operation at the instant load current. Then, the output, input and inductor currents settle at their due average values. If the inductor works in the weak saturation region, the inductance is almost equal to $L_{\rm nom}$ and the peak-to-peak ripple current $\Delta i_{L\rm pp} = I_{L,\rm peak} - I_{L,\rm valley}$ can be approximated by

$$\Delta i_{L\rm pp} = \frac{(V_{\rm in} - V_{\rm out})V_{\rm out}}{f_s L_{\rm nom} V_{\rm in}}. \tag{1}$$

The magnitude of $\Delta i_{L\rm pp}$ affects size and losses of the inductor and of other power components (e.g. MOSFETs and capacitors), as well as peak current mode control operation (e.g. slope compensation) and current limit setting and action. Equation (1) can be reversed to determine the desired inductance $L_{\rm des}$, required to achieve a certain maximum ripple current $\Delta i_{L\rm ppmax}$, given by

$$L_{\rm des} = \frac{(V_{\rm in} - V_{\rm out})V_{\rm out}}{f_s V_{\rm in} \Delta i_{L\rm pp\,max}}. \tag{2}$$

Equations (1) and (2) make the steady-state analysis and design easy and straightforward, and simplified formulas for winding and core loss calculation [30]–[32] can be adopted to verify

the inductor compliance with converter specifications. In common design practice, inductors are chosen in such a way they can work in the weak saturation region, even in worst-case operations, and the typical adopted value of $\Delta i_{L\mathrm{ppmax}}$ is about 40% of the dc average current $I_{L,\mathrm{av}}$ [33], [34]. So, it seems that working in weak saturation region makes the SMPS design quite comfortable. However, some questions are legitimate.

1) Do we really need to keep inductors working in the weak saturation region?
2) Which is the most appropriate position of the dc average current $I_{L,\mathrm{av}}$ of the inductor over the *L* versus *I* curve?
3) Which is the most appropriate value of $Di_{L\mathrm{ppmax}}$?

The answer to question 1 is subordinated to the answers to questions 2 and 3. Saturation is a progressive reduction of the inductance versus the increase of the winding current. Depending on the type of magnetic core, the inductance roll-off can be sharper or smoother. Strictly speaking, a unique value for saturation current does not exist. Manufacturers provide the values of currents determining 10%, 30%, or 50% inductance drops with respect to its nominal value L_{nom}, or curves like the one in Fig. 2. The depth of inductance drop is directly related to the magnitude of the magnetic flux density *B* inside the core material. In order to figure out the correlation between the magnetic flux density and the main core characteristics, let us refer to the simpler case of a gapped linear inductor (having fixed permeability). For an inductor with gapped core, the inductance and the resulting magnetic flux density are given by

$$L = \frac{n^2}{\Re_g + \Re_c} = \frac{n^2}{\frac{l_g}{\mu_o A_c} + \frac{l_c}{\mu_c A_c}} = \frac{n^2 \mu_o A_c}{l_g + \frac{l_c}{\mu_r}} \tag{3a}$$

$$B = \frac{n\, i_L}{(\Re_g + \Re_c)\, A_c} = i_L \sqrt{\mu_o L / \left(l_g + \frac{l_c}{\mu_r}\right) A_c} \tag{3b}$$

where $l_g >> l_c/\mu_r$. For large air gaps, the permeance of other field paths out of the air gap is not negligible. It results in much larger values for *L* than predicted by (3a). In [8] and [35], analytical approximations for fringing flux calculations around the air gaps of inductor cores are proposed, and in [31] a complete analysis on gapped inductor formulas can be found.

If we wish to operate with a given inductance *L*, from (3b), the inductance drop at a given current i_L can be reduced by taking a core either with bigger cross section A_c, or with bigger gap length l_g, or both. In the first case, bigger cross section A_c means that the core is bigger. Total core and winding losses may as increase as decrease, because of the overall balance among the decrease of magnetic flux density ac component, the increase of the core volume, and the increase of the turns mean length. In the second case, if the core is unchanged, the copper losses necessarily increase, due to the higher number of turns required to keep fixed the inductance value. From (3b), it also follows that a lower inductance *L* might help in reducing the magnetic flux density. However, lower inductance means bigger ripple $\Delta i_{L\mathrm{pp}}$ and higher winding and core losses [7]. Therefore, there is no guarantee that a bigger inductor with bigger inductance ensures both lower saturation and lower losses than a smaller inductor with smaller inductance. The best choice is to take an inductor with the smallest possible core and inductance leading to acceptable losses and temperature conditions, including possible operation in the roll-off region.

Whatever region the inductor is operating in, the key problem is to determine the correct value of $\Delta i_{L\mathrm{pp}}$, in order to achieve a consequent reliable and joint prediction of losses and temperature rise. One possible way is given by using a circuit simulator enabling the use of nonlinear inductor models. The main drawback of this approach is the need to run a circuit transient, requiring a possible long time for reliable simulation setup and execution. In this paper, a different approach is proposed for the prediction of the ripple $\Delta i_{L\mathrm{pp}}$.

A. Proposed Model

Dynamic inductance versus winding current (*L* versus *I*) curves provided by different manufacturers can cover different ranges of current. The *L* versus *I* curves of FC inductors can be analytically described by means of an arctangent function, defined as follows:

$$L\left[i_L(t)\right] = L_{\mathrm{deepsat}} + \frac{L_{\mathrm{nom}} - L_{\mathrm{deepsat}}}{2}\left\{1 - \frac{2}{\pi}\tan^{-1}\left\{\sigma\left[i_L(t) - I_L^*\right]\right\}\right\} \tag{4}$$

where σ is a smoothness factor representing the rate of the inductance roll-off for increasing current. Both σ and I_L^* are temperature-dependent parameters, as later discussed in Section III. The values of L_{nom} and L_{deepsat} are readable from datasheets and/or from the inductances curves provided by manufactures. The values of σ and I_L^* are usually not directly available, but they can be obtained by applying (4) for two current values $i_L(t) = I_{\alpha\%}$ and $i_L(t) = I_{\beta\%}$, corresponding to the $\alpha\%$ drop and the $\beta\%$ drop of inductance with respect to the nominal value L_{nom}, namely $L_{\alpha\%}$ and $L_{\beta\%}$. Any couple of percent drops between 10% and 90% can be adopted, if the inductances curves are provided in the manufactures' datasheets. According to (4), given $i_L(t) = I_{30\%}$ and $i_L(t) = I_{70\%}$, the values of σ and I_L^* can be calculated by

$$\sigma = \frac{\cot\left(\pi\,\Gamma_{30\%}\right) - \cot\left(\pi\,\Gamma_{70\%}\right)}{I_{30\%} - I_{70\%}} \tag{5a}$$

$$I_L^* = \frac{I_{70\%}\cot\left(\pi\,\Gamma_{30\%}\right) - I_{30\%}\cot\left(\pi\,\Gamma_{70\%}\right)}{\cot\left(\pi\,\Gamma_{30\%}\right) - \cot\left(\pi\,\Gamma_{70\%}\right)} \tag{5b}$$

$$\Gamma_{30\%} = \frac{L_{30\%} - L_{\mathrm{deepsat}}}{L_{\mathrm{nom}} - L_{\mathrm{deepsat}}};\ \Gamma_{70\%} = \frac{L_{70\%} - L_{\mathrm{deepsat}}}{L_{\mathrm{nom}} - L_{\mathrm{deepsat}}} \tag{5c}$$

where $L_{30\%}$ and $L_{70\%}$ correspond to the 30% drop and the 70% drop of the nominal inductance value L_{nom}, respectively. According to (4), L_{nom} represents the mathematical asymptote of the function $L(i_L)$ for $i_L \to -\infty$. But L_{nom} cannot be measured in practice. Based on the industry standards, the value used by manufacturers for L_{nom} is the one closest to the inductance value measurable at $i_L \cong 0$. The approximation $L(i_L = 0) \cong L_{\mathrm{nom}}$ allows us to simplify the σ and I_L^* parameters identification and provides good results for practical purposes. Indeed, the error on L_{nom} involved by such an approximation is lower than 10%, which is within the uncertainty declared by manufacturer for

$L_{\rm nom}$ (about 20–30%). From (4), we obtain

$$v_L(t) = L\left(i_L(t)\right)\frac{di_L(t)}{dt} = L_{\rm deepsat}\frac{di_L(t)}{dt} + \frac{L_{\rm nom}-L_{\rm deepsat}}{2}\left\{1-\frac{2}{\pi}\tan^{-1}\left\{\sigma\left[i_L(t)-I_L^*\right]\right\}\right\}\frac{di_L(t)}{dt}. \quad (6)$$

As the voltage v_L is constant over the two CCM switching-mode operation intervals [see Fig. 1(b)], it is

$$\int_{t_1}^{t_2} v_{L,x}(t)dt = V_{L,x}(t_2-t_1) = \int_{t_1}^{t_2} L\left[i_L(t)\right]\frac{di_L(t)}{dt}dt \quad (7)$$

where $x = r$ if $t \in [0, DT_s)$ and $x = f$ if $t \in [DT_s, T_s)$. From (7), it follows that

$$-V_{L,r}\cdot t + \frac{L_0+L_{\rm deepsat}}{2}\left[i_{L,r}(t)-i_{L0}\right] - \frac{L_0-L_{\rm deepsat}}{\pi}\left[y(t)-y_0\right] = 0 \quad (8a)$$

for $t_1 = 0$ and $t_2 = t[0, DT_s)$ and

$$-V_{L,f}\cdot(t-DT_s) + \frac{L_0+L_{\rm deepsat}}{2}\left[i_{L,f}(t)-i_{LD}\right] - \frac{L_0-L_{\rm deepsat}}{\pi}\left[y(t)-y_D\right] = 0 \quad (8b)$$

for $t_1 = DT_s$ and $t_2 = t[DT_s, T_s)$, where $L_0 = L(i_{L0})$, $y_0 = y(t=0)$, $y_D = y(t=DT_s)$, $i_{L,r}$ and $i_{L,f}$ are the rising and falling inductor currents in $[0, DT_s)$ and $[DT_s, T_s)$, respectively, and the function $y(t)$ is defined as follows:

$$y(t) = \int \tan^{-1}\left\{\sigma\left[i_L(t)-I_L^*\right]\right\}\frac{di_L}{dt}dt = \left[i_L(t)-I_L^*\right]\tan^{-1}\left\{\sigma\left[i_L(t)-I_L^*\right]\right\} - \frac{\log\left\{1+\sigma^2\left[i_L(t)-I_L^*\right]^2\right\}}{2\sigma}. \quad (9)$$

Equations (8a) and (8b) are not enough to determine the inductor current wave-shape. First, the inductor current in $t = 0$ and $t = DT_s$ are not known in advance: consequently, according to (9), y_0 and y_D cannot be evaluated without i_{L0} and i_{LD}. But, also supposing to know the values of inductor current i_{L0} and i_{LD}, (8a) and (8b) cannot be solved in analytical form to determine the value of the inductor current $i_{L,x}(t)$ at any instant t. For a given time interval $[t_a, t_b]$, each equation can be solved only in numerical form: in particular, under the hypothesis that $i_L(t_a)$ is known, a root-finding algorithm can be adopted to find the value of $i_L(t_b)$. Let us now see how we can apply this numerical model to the determination of the FC inductor current wave-shape.

B. Proposed Algorithm

Fig. 3 shows the typical current wave-shape for a saturated inductor into a switching converter in steady-state operation. A good representation of the inductor current wave-shape within [0, DT_s) and [DT_s, T_s) time intervals can be achieved by five samples, taken in the following instants:

- the starting instant t_s;
- the ending instant t_e;
- the middle instant t_m, given by the intersection of the tangents in t_s and t_e;
- the left middle instant t_{lm}, given by the intersection of the tangents in t_s and t_m;
- the right middle instant t_{rm}, given by the intersection of the tangents in t_m and t_e.

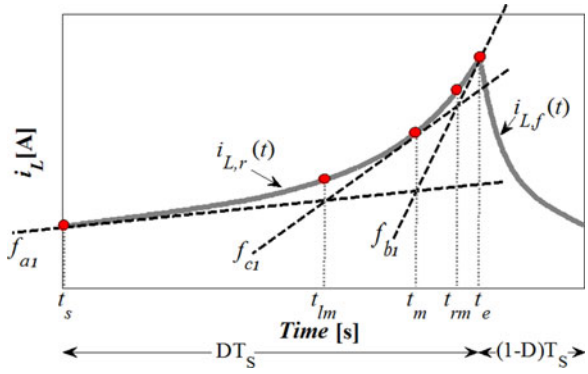

Fig. 3. Typical saturated wave-shape for an FC inductor.

Samples and corresponding time instants are shown for the time interval [0, DT_s] in Fig. 3. The flow diagrams given in Fig. 4 summarize the entire procedure to calculate the five samples of the inductor current over the switching period.

Let us refer to the time interval [0, DT_s]. Thus, $t_s = 0$ and $t_e = DT_s$. Let us suppose that the inductor current $i_L(t_s) = i_{L0}$ is known. Given i_{L0}, the Newton–Raphson algorithm can be applied to (8a) to find the value $i_L(t_e) = i_{LD}$. The tangents to the inductor current in t_s and t_e intersect each other at the time instant t_m. Given i_{L0}, the Newton–Raphson algorithm can be applied again to (8a) to find the value of $i_L(t_m)$. Then, the tangents to the inductor current in t_s and t_m and in t_m and t_e can be determined. They intersect each other in correspondence of the time instants t_{lm} and $t_{\rm rm}$, respectively. Finally, applying the Newton–Raphson algorithm to (8a), $i_L(t_{lm})$ and $i_L(t_{\rm rm})$ can be found. Thus, the five samples within [0, DT_s] are obtained. A similar approach can be used to obtain the current samples and the corresponding time instants t_s, t_{lm}, t_m, $t_{\rm rm}$, and t_e in the interval $[DT_s, T_s]$, applying the Newton–Raphson algorithm to (8b). For each current sample, (4) provides the relevant inductance. Evidently, all samples can be calculated starting from the value of i_{L0}. Given the operating conditions ($V_{\rm in}$, $V_{\rm out}$, $I_{\rm out}$, f_s) and the inductors parameters (L_{nom}, σ, I_L^*), the calculation of i_{L0} and i_{LD}, and the resulting current ripple, can be achieved by means of the flow diagram shown in Fig. 5.

The algorithm of Fig. 5 starts from a guess value $i_{L0,\rm guess}$ for i_{L0}, obtained from the assumption that the inductor is in weak saturation, and then, its current has an almost triangular wave-shape. Accordingly, a possible guess value of the inductor current ripple $\Delta i_{L\rm pp,guess}$ is given by (1), assuming $L_{\rm nom} = L(I_{L,\rm av})$.

The resulting $i_{L0,\rm guess}$ value is given by

$$i_{L0,\rm guess} = I_{L,\rm av} - \frac{1}{2}\Delta i_{L\rm pp,guess}. \quad (10)$$

If the converter operates in steady state with output voltage regulation, then the inductor average current fulfills the

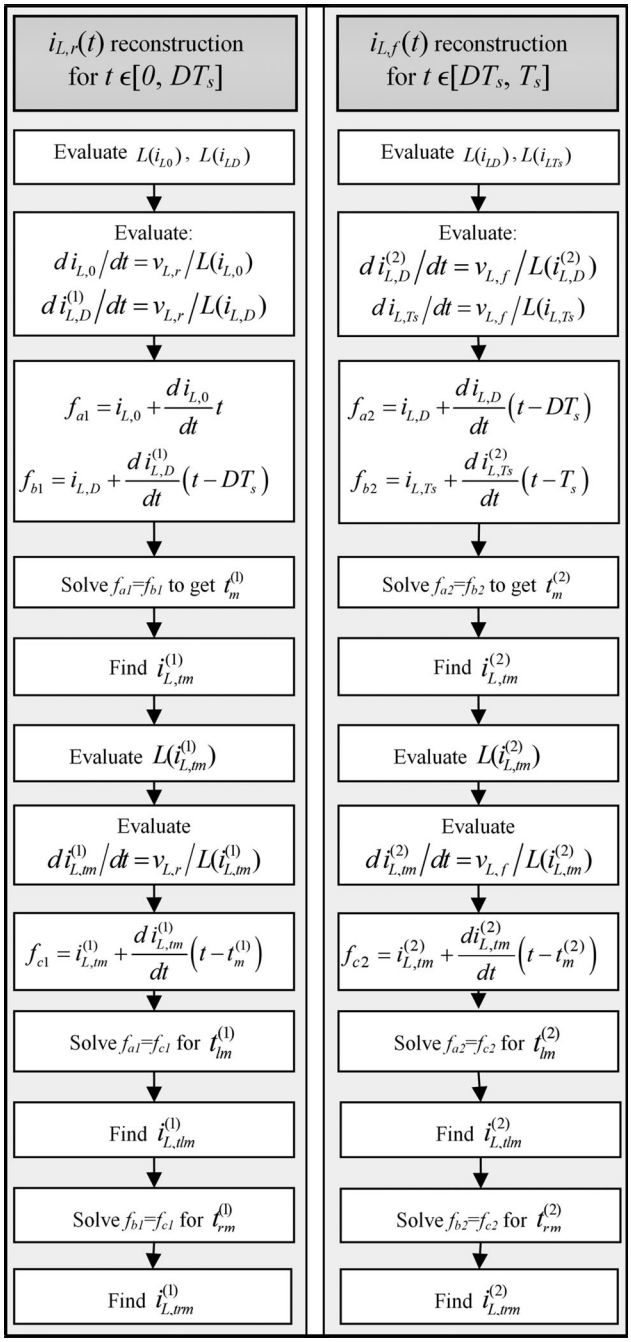

Fig. 4. Algorithm for inductor current wave-shape reconstruction.

equation:

$$f_s \int_0^{T_s} i_L(t)dt = I_{L,\mathrm{av}}. \tag{11}$$

Accordingly, using the current samples specified above, we can impose that

$$f_s \int_0^{T_s} i_L(t)dt \simeq \frac{1}{2} f_s \left(\Psi_r + \Psi_f\right) = \tilde{I}_{L,\mathrm{av}} \tag{12}$$

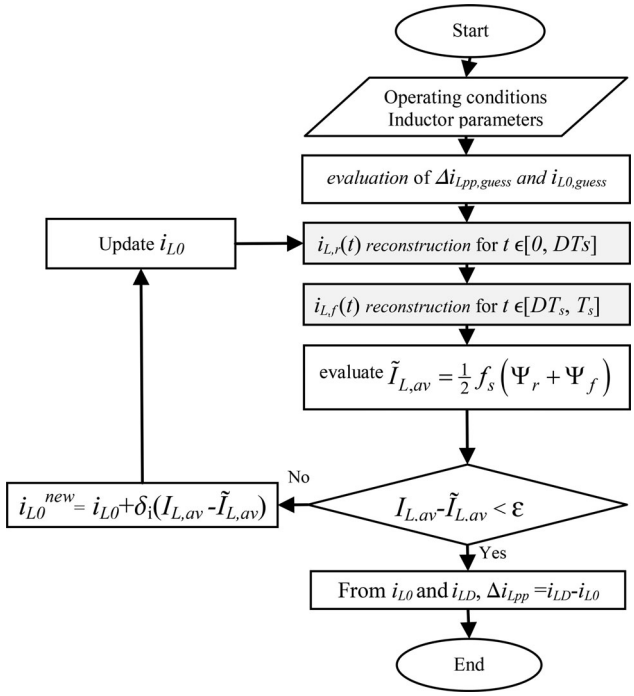

Fig. 5. Proposed algorithm for inductor current ripple evaluation.

where

$$\begin{aligned}\Psi_x = &\left(i_{L,t_s}^{(x)} + i_{L,t_{lm}}^{(x)}\right)\left(t_{lm}^{(x)} - t_s^{(x)}\right) + \left(i_{L,t_{lm}}^{(x)} + i_{L,t_m}^{(x)}\right) \\ &\times \left(t_m^{(x)} - t_{lm}^{(x)}\right) + \left(i_{L,t_m}^{(x)} + i_{L,t_{rm}}^{(x)}\right)\left(t_{rm}^{(x)} - t_m^{(x)}\right) \\ &+ \left(i_{L,t_{rm}}^{(x)} + i_{L,t_e}^{(x)}\right)\left(t_e^{(x)} - t_{rm}^{(x)}\right)\end{aligned} \tag{13}$$

with $x = r$ if $t \in [0, DT_s)$ and $x = f$ if $t \in [DT_s, T_s)$. For each iteration of the algorithm given in Fig. 5, the difference between $I_{L,\mathrm{av}}$ and $\tilde{I}_{L,\mathrm{av}}$ is determined, and if lower than a minimum acceptable error ε (e.g., $\varepsilon = 0.001$), then the loop is terminated; otherwise, the value of i_{L0} is updated as $i_{L0}^{\mathrm{new}} = i_{L0} + \delta_i(I_{L,\mathrm{av}} - \tilde{I}_{L,\mathrm{av}})$, where the gain δ_i determines the convergence speed and the stability of the algorithm ($\delta_i = 0.1$ is a fair conservative choice).

C. Examples

Let us consider the MSS7341-183ML Coilcraft part with $L_{\mathrm{nom}} = 18$ μH [36]. For a buck converter with $V_{\mathrm{in}} = 12$ V, $V_{\mathrm{out}} = 3.3$ V, $f_s = 465$ kHz and $I_{\mathrm{out}} = [0.5, 3.75]$ A, the resulting currents and inductance wave-shapes yield by the proposed algorithm are shown in Fig. 6. Plots of Fig. 6(a) highlight that the inductor current waveshape looks triangular below $l_{\mathrm{Lav}} = 1.5$ A and above $l_{\mathrm{Lav}} = 2.75$ A. Average inductor current $I_{L\mathrm{av}}$. The expected cusp wave-shape of a saturated inductor current appears only for values of the average current between these two boundaries. Indeed, the inductor works in weak saturation region when the average current is much smaller than I_L^* [see Fig. 7(a)], while the inductor mainly works in the deep saturation region when the average current is much bigger than I_L^* [see Fig. 7(c)]. As discrete FC inductors are built using

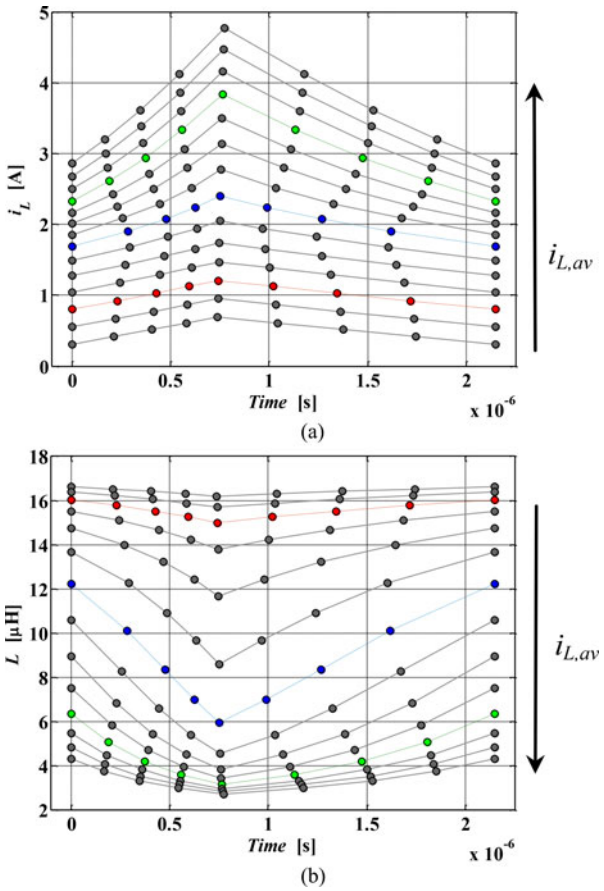

Fig. 6. (a) Current and (b) inductance wave-shapes for MSS7341-183ML at different values of the current $I_{L,\mathrm{av}}$. According to the versus of the current arrow, $I_{L,\mathrm{av}}$ moves from 0.5 to 3.75 A, using steps of 0.25 A.

gapped cores, the gap limits the inductance, making it larger than the air inductance, though not as much as the same ungapped core would allow [23]. As a result, Fig. 6(b) shows that the inductance is lower than 6 μH when the inductor works in deep saturation region (e.g., at $I_{L\mathrm{av}} = 3$ A), whereas the inductance is about 15 μH when the inductor works in the weak saturation region (e.g., at $I_{L\mathrm{av}} = 1.0$ A). Accordingly, the peak-to-peak current ripple of the deeply saturated inductor is about five times the ripple resulting for the weakly saturated inductor. In Fig. 6(a), the wave-shapes of the inductor working with at an average current such that the ripple falls within the roll-off region are also shown. In such situation, the peak-to-peak current ripple can be bigger than the ripple at the nominal inductance, though not so much as someone could expect. For example, at $I_{L\mathrm{av}} = 2$ A, the peak-to-peak ripple is $\Delta i_{L\mathrm{pp}} = 0.68$ A ($\Delta i_{L\mathrm{pp}}/I_{L\mathrm{av}} \approx 34\%$), whereas at $I_{L\mathrm{av}} = 1$ A, the peak-to-peak ripple is $\Delta i_{L\mathrm{pp}} = 0.42$ A ($\Delta i_{L\mathrm{pp}}/I_{L\mathrm{av}} \approx 42\%$). Therefore, despite of the saturation, $I_{L\mathrm{av}} = 2$ A could be an acceptable operating current for the inductor, provided that the power losses and the temperature of the part are within the allowed limits, and the inductor current ripple does not cause bad operation of the other power devices, such as MOSFETs and capacitors. Nevertheless, a complete analysis of the inductor, including the thermal dependence of parameters, is required in order to predict the realistic behavior of the device in whatever operating condition.

III. Temperature Impact on Inductor Saturation

In the SMPS design, data describing overall impact of temperature on power devices losses and temperature are needed. The temperature effects on the inductors winding resistance at low and high frequencies are deeply discussed in the literature [37]. Thermal effects on hysteresis of soft ferrites are also discussed in the literature [38], [39]. Some manufacturers provide data and/or curves describing the changes of the L versus I curves with respect to the temperature. As shown in Fig. 8, a temperature increase determines a decrease of I_L^*, an increase of L_0 and of the roll-off steepness in FC inductors. Complete data regarding all these dependences are not always disclosed by manufacturers. Mostly, the curves available in datasheets and websites show a horizontal left-side drift of the curves when the temperature increases. Starting from the experimental L versus I curves of FC inductors working at different temperatures, the thermal coefficients $\lambda_{30\%}$ and $\lambda_{70\%}$ can be determined for the current values $I_{30\%}$ and $I_{70\%}$, given by

$$\lambda_{30\%} = \frac{\left(\dfrac{I_{30\%,T} - I_{30\%,25^\circ\mathrm{C}}}{I_{30\%,25^\circ\mathrm{C}}}\right)}{T - 25^\circ}, \tag{14a}$$

$$\lambda_{70\%} = \frac{\left(\dfrac{I_{70\%,T} - I_{70\%,25^\circ\mathrm{C}}}{I_{70\%,25^\circ\mathrm{C}}}\right)}{T - 25^\circ} \tag{14b}$$

From (14), the temperature effect on $I_{30\%}$ and $I_{70\%}$ can be evaluated as follows:

$$I_{30\%}(T) = I_{30\%,25^\circ\mathrm{C}}\left[1 + \lambda_{30\%}(T - 25^\circ)\right] \tag{15a}$$

$$I_{70\%}(T) = I_{70\%,25^\circ\mathrm{C}}\left[1 + \lambda_{70\%}(T - 25^\circ)\right] \tag{15b}$$

Therefore, from (15), the updated temperature-dependent values of σ and I_L^* can be determined by means of (5b).

IV. Experimental Results

The experimental tests have been realized by using the Texas Instruments TPS54160EVM–230 buck converter evaluation board [40]. The following case study has been investigated and discussed: $V_{in} = 12$ V, $V_{out} = 3.3$ V, $l_{out} = [1.5; 2.1]$ A, $f_s = 465$ kHz. (at about 20 °C ambient temperature). The MSS7341-183ML inductor has been connected to the board through a pair of wires allowing the connection of a current probe, as shown in Fig. 9. The comparison between the actual saturation curve and the modeled curve obtained by using the arctangent function given in (4) has been shown in Fig. 10 for such an inductor.

The instrumentation used for the experimental measurements includes a LeCroy WaveRunner 44Xi Oscilloscope, a Tektronix TCP 305 50A current probe with TCP A300 amplifier, a Sorensen Electronic Load, a Ti EX354RT Power Supply and a Fluke 54 II B digital thermometer with K type thermocouple have been adopted for the experimental measurements. For the MSS7341-183ML part, L_{nom} and L_{deepsat} have been extracted from the datasheet; σ and I_L^* have been evaluated using (5a) and

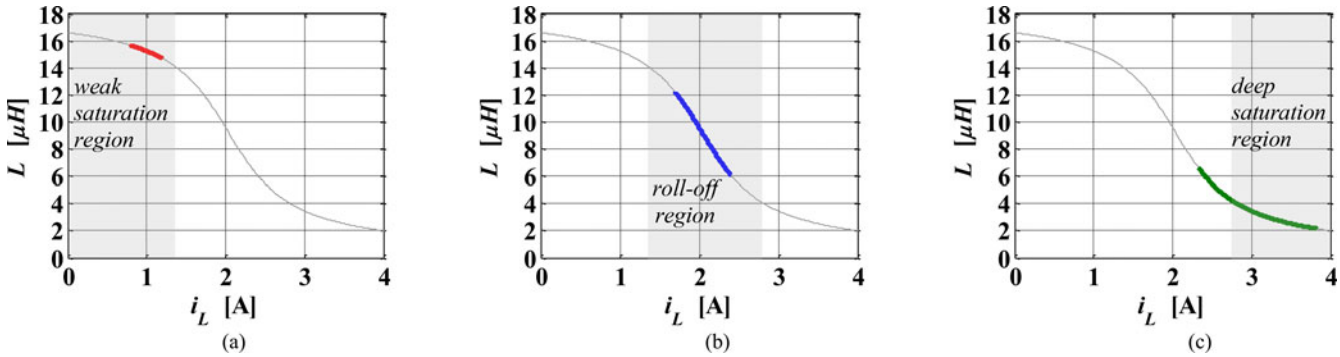

Fig. 7. Inductance vs current curves (gray curves) and different inductor current swings (red, blue and green thick curve) for MSS7341-183ML: $I_{L,\mathrm{av}} = 1.0$ A (a), $I_{L,\mathrm{av}} = 2.0$ A (b), $I_{L,\mathrm{av}} = 3.0$ A (c).

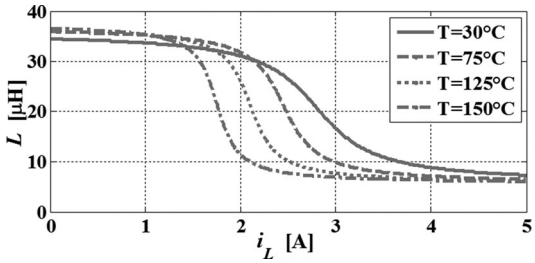

Fig. 8. Temperature influence on the *L* versus *I* curve for an FC inductor.

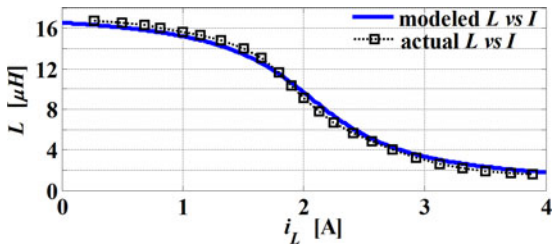

Fig. 10. Modeled and actual saturation curve for MSS7341-183ML.

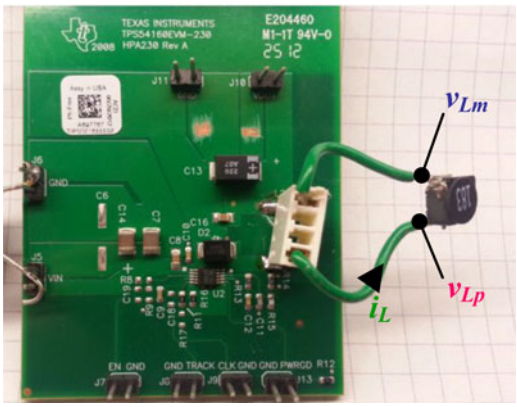

Fig. 9. Evaluation board adopted for the experimental test.

(5b), respectively. Thermal coefficients, like $\lambda_{30\%}$, $\lambda_{70\%}$, and λ_{DCR}, have been evaluated using the *L* versus *I* curves and the approximated formulas provided by the manufacturer. Fig. 11 shows the experimental measurements for the inductor voltages v_{Lp} and v_{Lm}, and the inductor current i_L, for $I_{L,\mathrm{av}} = 1.5$ A and $I_{L,\mathrm{av}} = 2.1$ A, respectively. Fig. 12 shows the ripple current measurements (green curves) and the simulation results obtained by using the proposed algorithm (red circles), respectively, for $I_{L,\mathrm{av}} = 1.5$ A and $I_{L,\mathrm{av}} = 2.1$ A.

A further experimental test has been conducted by using a 15 μH part. Similarly, the MSS7341-153ML inductor has been connected to the board. Fig. 13 shows the experimental measurements for the inductor voltages v_{Lp} and v_{Lm}, and the inductor current i_L, respectively for $I_{L,\mathrm{av}} = 1.5$ A and

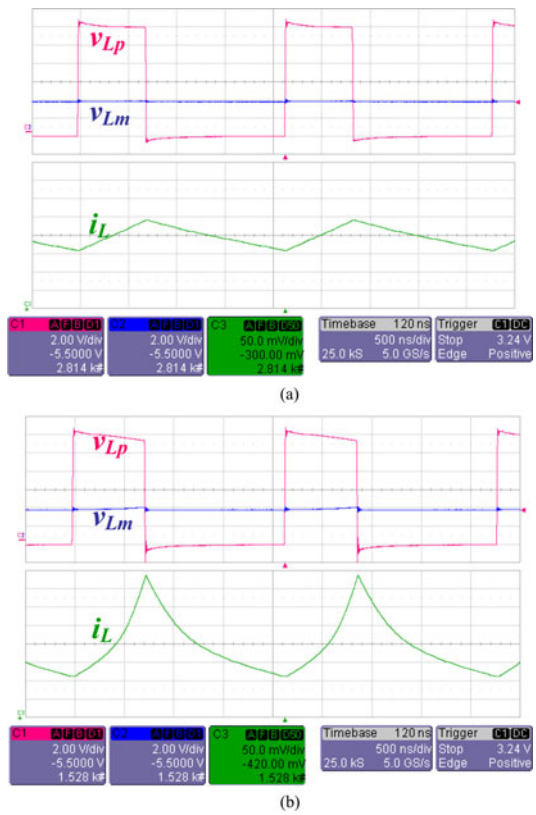

Fig. 11. MSS7341-183 part: voltages and currents experimental measurements (current amplification applied = x5). (a) $I_{L,\mathrm{av}} = 1.5$ A. (b) $I_{L,\mathrm{av}} = 2.1$ A.

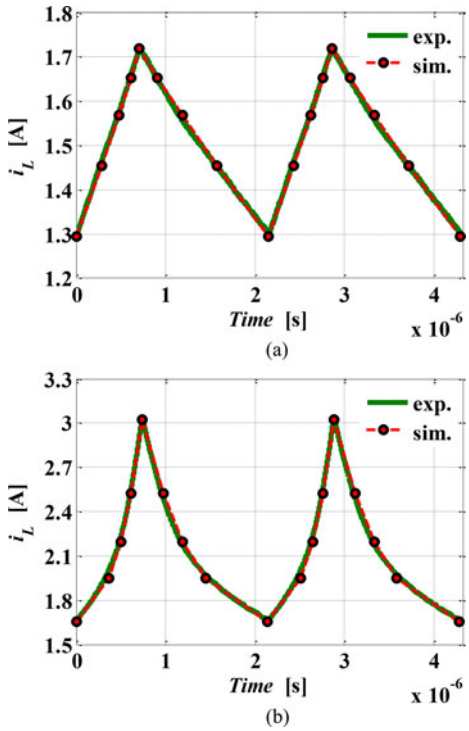

Fig. 12. MSS7341-183 part: simulated (red-dashed lines with red dots) and measured (green wave-shapes) inductor current ripple. (a) $I_{L,\mathrm{av}} = 1.5$ A. (b) $I_{L,\mathrm{av}} = 2.1$ A.

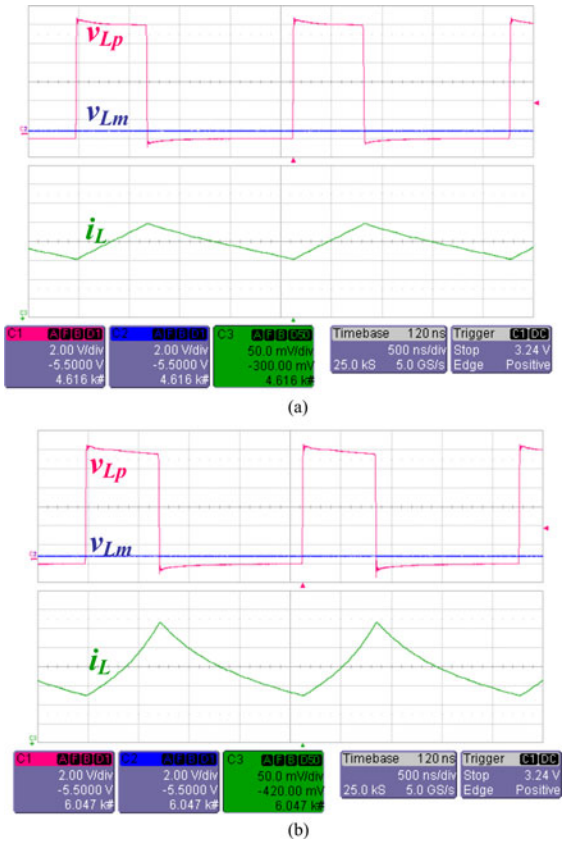

Fig. 13. MSS7341-153 part: voltages and currents experimental measurements (current amplification applied = x5). (a) $I_{L,\mathrm{av}} = 1.5$ A. (b) $I_{L,\mathrm{av}} = 2.1$ A.

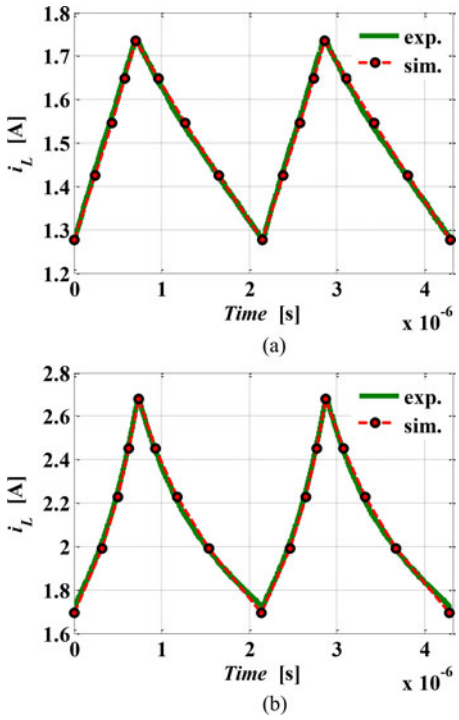

Fig. 14. MSS7341-153 part: simulated (red-dashed lines with red dots) and measured (green wave-shapes) inductor current ripple (a) $I_{L,\mathrm{av}} = 1.5$ A (b) $I_{L,\mathrm{av}} = 2.1$ A.

$I_{L,\mathrm{av}} = 2.1$ A. Once again, Fig. 14 shows the ripple current measurements (green curves) and the simulation results (red circles), respectively, for $I_{L,\mathrm{av}} = 1.5$ A and $I_{L,\mathrm{av}} = 2.1$ A. The waveforms shown in Figs. 12 and 14 highlight a perfect agreement between experimental and simulated ripple waveforms. These experimental results validate the model and the method for the analysis of inductors operating in saturation presented in the previous sections. Thanks to the reconstruction of the ripple current waveform, it could be possible to correctly evaluate as the copper losses, including the effects of high frequency harmonics, as the core losses, which are dependent on the peak-to-peak ripple current too. This analysis is very significant as in the design of high-power-density converters, as in the identification of main inductor parameters from experimental measurements.

V. Conclusion

A smart use of inductors in the SMPS design requires an aware assessment of inductor saturation effects. The lack of methods for quick prediction of real impact of inductor saturation in SPMS applications leads designers to the conservative choice of bigger inductors, aspiring lower ripple, losses, and temperature rise, whereas sometimes a smaller inductor could globally outperform a bigger one. The model and method for ripple analysis of saturated inductors proposed in this paper allow the investigation of effective SMPS design solutions with minimum size inductors, as well as the identification of optimum design tradeoff and of the parameters of the inductors. The proposed algorithm has been fully validated experimentally, with highly accurate reconstruction of current ripple.

REFERENCES

[1] C.O. Mathúna, N. N. Wang, S. Kulkarni, and S. Roy, "Review of integrated magnetics for power supply on chip (PwrSoC)," *IEEE Trans. Power Electron.*, vol. 27, no. 11, pp. 4799–4816, Nov. 2012.

[2] D.S. Gardner, G. Schrom, F. Paillet, B. Jamieson, T. Karnik, and S. Borkar, "Review of on-chip inductor structures with magnetic films," *IEEE Trans. Magn.*, vol. 45, no. 10, pp. 4760–4766, Oct. 2009.

[3] P. Herget, N. Wang, E. J. O'Sullivan, B. C. Webb, L. T. Romankiw, R. Fontana, G. Decad, and W. J. Gallagher, "Limits to on-chip power conversion with thin film inductors," *IEEE Trans. Magn.*, vol. 49, no. 7, pp. 4137–4143, Jul. 2013.

[4] D. W. Lee, K.-P. Hwang, and S. X. Wang, "Fabrication and analysis of high-performance integrated solenoid inductor with magnetic core," *IEEE Trans. Magn.*, vol. 44, no. 11, pp. 4089–4095, Nov. 2008.

[5] C. R. Sullivan and S. R. Sanders, "Design of micro-fabricated transformers and inductors for high-frequency power conversion," *IEEE Trans. Power Electron.*, vol. 11, no. 2, pp. 228–238, Mar. 1996.

[6] A. De Nardo, G. Di Capua, and N. Femia, "Transformer design for isolated switching converters based on geometric form factors of magnetic cores," *IEEE Trans. Ind. Electron.*, vol. 60, no. 6, pp. 2158–2166, Jun. 2013.

[7] A. Van De Bossche and V. Cekov Valchev, *Inductors and Transformers for Power Electronics*. New York, NY, USA: Taylor & Francis, 2005.

[8] C. W. T. McLyman, *Transformer and Inductor Design Handbook*, 2nd ed. New York, NY, USA: Marcel Dekker, 1988.

[9] E. C. Snelling, *Soft Ferrites: Properties and Applications*, 2nd ed. Oxford, U.K.: Butterworths, 1988.

[10] N. J. Schade, "Core Losses in Composite Inductors", *Design Handbook*, Vishay Intertech., Inc. [Online]. Available: http://ecadigitallibrary.com/pdf/CARTSEUROPE06/3.6% 20Shade a.pdf.

[11] N. Garcia, *Power Inductor and Peak Current Handling Capability*. Rockledge, FL, USA: Renco Electron., Jan. 2012.

[12] L. Crane, *Ferrite and Powder Core Materials for Power Inductors*. Cary, IL, USA: Coilcraft, Feb. 2006.

[13] R. A. Salas and J. Pleite, "Simulation of the saturation and air-gap effects in a pot Ferrite Core with a 2-D finite element model," *IEEE Trans. Magnet.*, vol. 47, no. 10, pp. 4135–4138, Oct. 2011.

[14] R. A. Salas and J. Pleite, "Equivalent electrical model of a Ferrite Core inductor excited by a square waveform including saturation and power losses for circuit simulation," *IEEE Trans. Magn.*, vol. 49, no. 7, pp. 4257–4260, Jul. 2013.

[15] A. Stadler, T. Stolzke, and C. Gulden, "Nonlinear power inductors for large current crest factors," in *Proc. Eur. Power Convers. Intell. Motion Conf.*, May 2012, pp. 1548–1553.

[16] L. Milner and G. A. Rincon-Móra, "Small saturating inductors for more compact switching power supplies," *IEEJ Trans. Elect. Electron. Eng.*, vol. 7, pp. 69–73, 2012.

[17] "*Derated L vs I Curves*", Coilcraft, Inc., 2014. [Online]. Available: http://www.coilcraft.com/apps/lattemp/lattemp.cfm

[18] *WE-PD HV SMD Power Inductor, #7687714221*, Würth, Künzelsau, Germany, Mar. 2014.

[19] J. Lu, H. Jia, X. Wang, K. Padmanabhan, W. G. Hurley, and Z. J. Shen, "Modeling, design, and characterization of multiturn bondwire inductors with ferrite epoxy glob cores for power supply system-on-chip or system-in-package applications," *IEEE Trans. Power Electron.*, vol. 25, no. 8, pp. 2010–2017, Aug. 2010.

[20] R. Meere, T. O'Donnell, H. J. Bergveld, N. Wang, N. Achotte, F. Rhen, and C. O'Mathuna, "Analysis of micro-inductor performance in a 20–100 MHz DC/DC converter," *IEEE Trans. Power Electron.*, vol. 24, no. 9, pp. 2212–2218, Sep. 2009.

[21] Q. Li, Y. Su, M. Mu, F. C. Lee, and D. Gilham, "Modeling of planar inductors with non-uniform flux distribution and non-linear permeability for high-density integration," in *Proc. 27th Annu. IEEE Appl. Power Electron. Conf. Expo.*, Feb. 2012, pp. 1002–1009.

[22] J. Cox, "Iron Powder Cores for Switch mode Power Supply Inductors". Micrometals Inc., [Online], Available: http://www.micrometals.com/appnotes/appnotedownloads/ipc4spsi.pdf

[23] J. D. Pollock, W. Lundquist, and C. R. Sullivan, "Predicting inductance roll-off with dc excitations," in *Proc. IEEE Energy Convers. Congr. Expo.*, Sep. 17–22, 2011, pp. 2139–2145.

[24] J. Lou, D. Reed, M. Liu, and N. X. Sun, "Electrostatically tunable magnetoelectric inductors with large inductance tenability," *Appl. Phys. Lett.*, vol. 94, no. 11, pp. 112508–1–112508-3, Mar. 2009.

[25] X. Fang, N. Zhang, and Z. L. Wang, "Converse magnetoelectric effects on heterotype electrostrain-piezopermeability composites," *Appl. Phys. Lett.*, vol. 93, no. 10, pp. 102503–102505, Sep. 2008.

[26] R.W. Schnell, R.A. Zane, and F. J. Azcondo, "Size reduction in low-frequency square-wave ballasts for high-intensity discharge lamps using soft-saturation magnetic material and digital control techniques," *IEEE Trans. Power Electron.*, vol. 28, no. 2, pp. 1036–1046, Feb. 2013.

[27] S. S. Ahsanuzzaman, T. McRae, M. M. Peretz, and A. Prodic, "Low-volume buck converter with adaptive inductor core biasing," in *Proc. 27th Annu. IEEE Appl. Power Electron. Conf. Expo.*, Feb. 5–9, 2012, pp. 335–339.

[28] R. A. Mastromauro, M. Liserre, and A. D. Aquila, "Study of the effects of inductor nonlinear behavior on the performance of current controllers for single-phase PV grid converters," *IEEE Trans. Ind. Electron.*, vol. 55, no. 5, pp. 2043–2052, May 2008.

[29] S. Mariethoz, M. Herceg, and M. Kvasnica, "Model predictive control of buck DC-DC converter with nonlinear inductor," in *Proc. 11th Workshop Control Modeling Power Electron.*, Aug. 17–20, 2008, pp. 1–8.

[30] A. M. Urling, V. A. Niemela, G. R. Skutt, and T. G. Wilson, "Characterizing high-frequency effects in transformer windings—A guide to several significant articles," *J. Circuits, Syst. Comput.*, vol. 5, pp. 607–626, Dec. 1996.

[31] A. Van den Bossche, V. C. Valchev, and G. B. Georgiev, "Measurement and loss model of ferrites with non-sinusoidal waveforms," in *Proc. IEEE 35th Power Electron. Spec. Conf.*, Jun. 20–25, 2004, pp. 4814–4818.

[32] J. Reinert, A. Brockmeyer, and R. W. A. A. De Doncker, "Calculation of losses in ferro- and ferrimagnetic materials based on the modified Steinmetz equation," *IEEE Trans. Ind. Appl.*, vol. 37, no. 4, pp. 1055–1061, Jul./Aug. 2001.

[33] S. Maniktala, *Switching Power Supply Design & Optimization*. New York, NY, USA: McGraw-Hill, May 2004.

[34] L.-G. He and J. Wu, "Selection of the current ripple ratio of converters and optimal design of output inductor," in *Proc. 5th IEEE Conf. Ind. Electron. Appl.*, Jun. 2010, pp. 1163–1167.

[35] A. Van den Bossche, V. Valchev, and T. Filchev, "Improved approximation for fringing permeances in gapped inductors," in *Proc. Conf. Rec. 37th Ind. Appl. Conf.*, Oct. 2002, vol. 2, pp. 932–938.

[36] Coilcraft, Inc., MSS7341 family datasheet, 2015 [Online]. Available: http://www.coilcraft.com/pdfs/MSS7341.pdf

[37] P. R. Wilson, J. N. Ross, and A. D. Brown, "Simulation of magnetic component models in electric circuits including dynamic thermal effects," *IEEE Trans. Power Electron.*, vol. 17, no. 1, pp. 55–65, Jan. 2002.

[38] L. Zegadi, J. J. Rousseau, B. Allard, P. Tenant, and D. Renault, "Model of power soft MnZn ferrites, including temperature effects," *IEEE Trans. Magn.*, vol. 36, no. 4, pp. 2022–2032, Jul. 2000.

[39] H.-Y. Lu, J. G. Zhu, and S. Y. R. Hui, "Measurement and modeling of thermal effects on magnetic hysteresis of soft ferrites," *IEEE Trans. Magn.*, vol. 43, no. 11, pp. 3952–3960, Nov. 2007.

[40] *TPS54160EVM-230-User's Guide, SLVU270*, Texas Instruments, Dallas, TX, USA, Sep. 2008.

Giulia Di Capua (S'06–M'13) received the B.S. and M.S. degrees (Hons.) in electronic engineering, and the Ph.D. degree in information engineering from the University of Salerno, Fisciano, Italy, in 2006, 2009, and 2013, respectively.

She is currently a research fellow at the University of Salerno. Her main research interest is design of isolated power converters in high-frequency high-efficiency applications.

Nicola Femia (M'94–SM'13) received the Laurea degree (Hons.) in industrial technologies engineering from the University of Salerno, in 1988.

He is Professor of Electrotechnics at the University of Salerno. His main research interests include optimization of high-energy-efficiency switching power supplies, power electronics for photovoltaic systems and renewable sources. He is the coauthor of more than 140 scientific papers published in international journals and in the proceedings of international symposia.

Mr. Femia was an Associate Editor for the IEEE TRANSACTIONS ON POWER ELECTRONICS from 1995 to 2003.